Assessing the Climate Impact of an Improved Volcanic Sulfate Aerosol Representation in E3SM

Ziming Ke[1], Qi Tang[1], Jean-Christophe Golaz[1], Xiaohong Liu[2], and Hailong Wang[3]

[1]Lawrence Livermore National Laboratory, Livermore, CA, USA

[2]Texas A&M University, College Station, TX, USA

[3]Pacific Northwest National Laboratory, Richland, WA, USA

Correspondence to: Ziming Ke (ke2@llnl.gov)

Abstract

Accurately simulating historical surface temperature variations is essential for evaluating climate models, yet many struggle to reproduce the mid-20th-century temperature trends associated with significant volcanic eruptions. This study examines the impact of volcanic sulfate aerosol representation on these biases using the Energy Exascale Earth System Model (E3SM). The standard CMIP6 protocol prescribes volcanic forcing through radiative perturbations, omitting volcanic aerosol-cloud interactions (VACIs). Here, we implement an emission-based approach with an updated volcanic eruption inventory that directly incorporates volcanic sulfur dioxide (SO_2) emissions, enabling a more process-based representation of volcanic forcing. This approach leads to improved surface temperature variability and a modest reduction in cold biases between 1940 and 1980 compared to the CMIP6 setup. Additionally, we assess cloud property responses to a more realistic volcanic sulfate aerosol representation, which weakens cloud-induced cooling during periods of lower volcanic activity. However, despite these refinements, a significant temperature cold bias remains, indicating that further improvements in atmospheric chemistry, aerosol microphysics, cloud processes, and model parameterizations are needed to fully resolve this issue in E3SM.

29
30
31
32   ## 1. Introduction
33   Volcanic eruptions play a crucial role in modulating climate changes (e.g. Chim et al., 2023; Hegerl et al., 2003).
34   Numerous studies have demonstrated their significant impacts on Earth's climate. For example, the eruption of
35   Tambora (Indonesia) in April 1815 led to the 'Year Without a Summer' of 1816 in Europe and North America —
36   which extended to several years in China—as well as severe disruptions to the Indian monsoon and to other global
37   climate patterns (Raible et al., 2016). The 1991 eruption of Mt. Pinatubo resulted in a peak top-of-the-atmosphere
38   radiative forcing of roughly 3-4 W/m2 and cooled global temperatures up to 0.4 °C (e.g. Dhomse et al., 2014; Mills
39   et al., 2017; Ramachandran et al., 2000; Rieger et al., 2020)
40
41   Intensive volcanic eruptions emit a variety of gases and particles into the stratosphere. The emitted sulfur dioxide
42   (SO_2) forms sulfate aerosols through atmospheric chemical reactions, which are the primary drivers of climate
43   perturbation (i.e. Dhomse et al., 2014; Mills et al., 2016). As lack of wet removal in the water-scarce stratosphere,
44   sulfate aerosols can persist for months to years compared to days in the troposphere (Mills et al., 2017). By
45   scattering incoming solar radiation, these sulfate aerosols induce cooling at the Earth surface while simultaneously
46   absorbing longwave radiation, thereby warming the surrounding air (Schmidt et al., 2018). This effect caused
47   specifically by volcanic sulfate aerosol is volcanic sulfate aerosol-radiation interactions (VARIs). Additionally, akin
48   to anthropogenic sulfate aerosols, volcanic sulfate particles can act as cloud condensation nuclei (CCN), facilitating
49   the formation of cloud droplets and changing of cloud albedo properties (Schmidt et al., 2012), resulting cloud
50   forcing enhancement. This is volcanic sulfate aerosol-cloud interactions (VACIs). The impact of VACIs on cloud
51   properties depends significantly on background aerosol conditions and regional meteorology. Chen et al. 2024 found
52   that volcanic eruptions in Hawaii led to a significant increase in cloud cover, enhancing reflected sunlight and
53   contributing to a substantial cooling effect. In contrast, Malavelle et al. 2017 examined volcanic sulfate aerosols near
54   Iceland and found that while cloud brightness increased, changes in cloud cover and liquid cloud water were
55   minimal. These differences highlight the complex interplay between volcanic sulfate injection, background cloud
56   droplet number concentration (CDNC), and regional cloud microphysics.
57
58   In the CMIP6 simulations, many climate models exhibit a mid-20th-century surface temperature cold bias, primarily
59   due to excessive cloud cooling effect associated with aerosol-cloud interactions (Flynn and Mauritsen, 2020; Zhang
60   et al., 2021). In E3SM version 2 (E3SMv2), this temperature bias becomes evident around 1940 and intensifies
61   following the 1963 Mt. Agung eruption (Golaz et al., 2022). The correlation between volcanic events and
62   temperature bias motivates our investigation into whether the model's volcanic sulfate aerosol treatment contributes
63   to this issue.
64
65   The CMIP6 protocol represents VARIs in the stratosphere using prescribed stratospheric aerosol optic properties
66   (Figure 1, left panel). During the satellite era, this approach blends multi-satellite observations, providing relatively
67   accurate representations of VARIs. However, it neglects VACIs, which can significantly influence cloud albedo and
68   radiative forcing. To address this limitation, we implement an emission-based approach, replacing prescribed
69   stratospheric aerosol optic properties with explosive volcanic SO2 emissions (Figure 1, right panel). This method,
70   which captures both VARIs and VACIs, has been validated in previous studies of volcano eruption events. (e.g.,
71   Brown et al., 2024; Mills et al., 2016).
72
73   To improve model initialization, we incorporate historical average volcanic SO2 emissions into pre-industrial (PI)
74   control simulations, establishing a different base line for subsequent historical transient simulations (1850–2014).
75   CMIP6 guidelines recommend including averaged natural forcing into PI control simulations (Eyring et al., 2016).
76   Schmidt et al. (2012) demonstrated that adding natural aerosols in PI and subsequent historical transient simulations
77   could potentially dampen the magnitude of the increase of aerosol-cloud interactions in the historical transient
78   period. Without volcanic sulfate aerosols, the ratio (R_0) of historical aerosol increases (A_a), which is mainly driven
79   by anthropogenic emission, relative to the PI average level (A_{PI}) is expressed as equation (1).
80
81       $$R_0 = \frac{A_a}{A_{PI}} \qquad (1)$$

82 When volcanic sulfate aerosols (A_v) are included, the new historical aerosol increase ratio, R_v, can be expressed as
83 equation (2), where $\overline{A_v}$ is historical average of volcanic sulfate aerosols.

84
$$R_v = \frac{A_a + A_v}{A_{PI} + \overline{A_v}} \qquad (2)$$

85
86 This simple algebraic relationship shows that the R_v is smaller than R_0. Since these ratios largely determines
87 historical cloud albedo change, a lower ratio suggests a weaker aerosol-cloud interaction and reduced cloud cooling
88 in historical transient simulations (Schmidt et al., 2012).
89
90 Furthermore, volcanic sulfate aerosols fluctuate over time, their effects on aerosol-cloud interaction and cloud
91 albedo also varies as a function of time. During periods of low volcanic activity, volcanic sulfate aerosols remain
92 below the historical average ($\overline{A_v}$), leading to a reduced R_v and a relative dimmed cloud cooling. Conversely, active
93 volcanic periods result in increased volcanic SO_2 emissions (strengthens A_v), resulting in larger R_v, and amplifying
94 aerosol-cloud interactions. These variations highlight the necessity of accurately representing volcanic aerosols in
95 climate simulations.
96
97 To evaluate this improved volcanic forcing treatment, we conducted new E3SMv2 simulations, including PI control
98 and transient simulations (1850–2014). The experimental setup is detailed in Section 2, results are presented in
99 Section 3, and conclusions follow in Section 4.
100
101
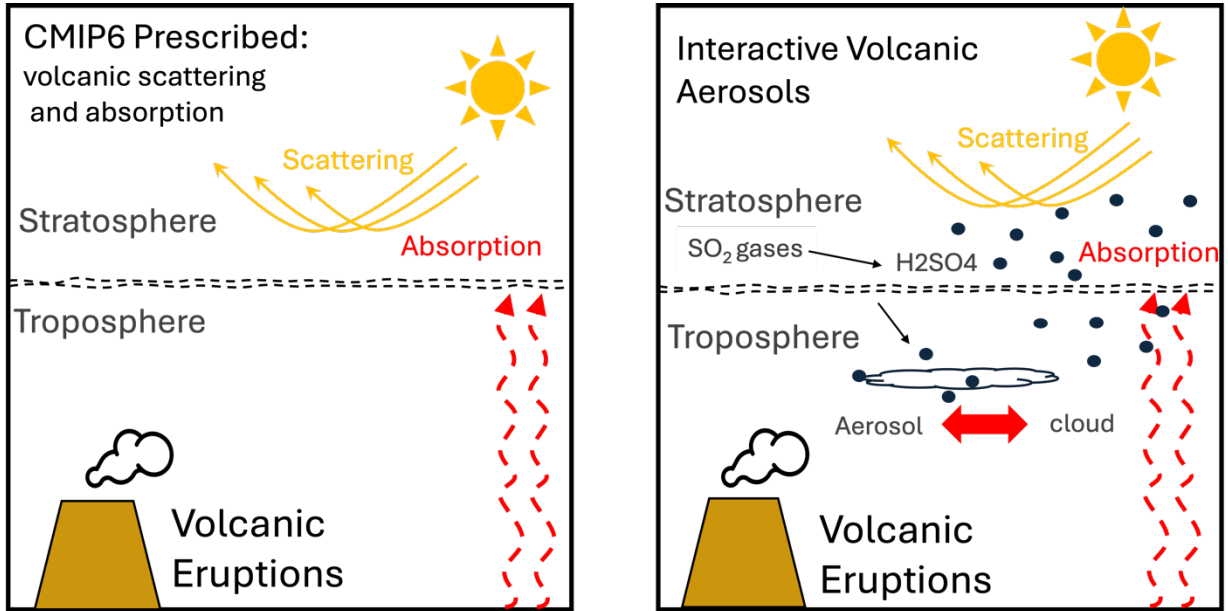
102
103
104 Figure 1. Volcanic forcing representations in E3SM: Prescribed stratospheric scattering and absorption following
105 CMIP6 protocol (left) and the interactive volcanic sulfate aerosols used in this study (right).
106
107
108
109
110 **2. Methods and Experiments**
111   2.1 The E3SM and Its Aerosol and Cloud Parameterizations
112 E3SMv2 is the state-of-the-art earth system model including a atmosphere model at 110 km horizontal resolution, a
113 land model at 165 km horizontal resolution, a 0.5°- horizontal resolution river routing model, and an ocean and sea
114 ice model with mesh spacing ranging from 60 km in mid-latitudes to 30 km at the equator and poles. The
115 atmosphere component, E3SM Atmosphere Model (EAM) v2, comprises 72 vertical layers extending to
116 approximately 60 km. Within EAMv2, the Cloud Layers Unified By Binormals (CLUBB) parameterization (Guo et

al., 2015) handles the subgrid turbulent transport and the macrophysics of stratiform and shallow cumulus clouds, while the planetary boundary layer (PBL) depth is diagnosed following the scheme by Holtslag and Boville (Holtslag and Boville, 1993). Deep convection is represented by a scheme developed by (Zhang and McFarlane, 1995), with an improved trigger function combining the dynamic Convective Available Potential Energy (dCAPE) trigger (Wang et al., 2020) and unrestricted air parcel launch level (ULL). Grid-scale cloud microphysical processes are parameterized using the version 2 of the Morrison and Gettelman (Morrison and Gettelman, 2008) microphysics scheme. E3SMv2 demonstrates enhanced performance compared to E3SMv1, with nearly double the computational speed and improvements in various metrics such as precipitation and cloud representation. Notably, its climate sensitivity is substantially lower, with an equilibrium climate sensitivity of 4.0 K, as opposed to the less plausible value of 5.3 K in E3SMv1. However, similar to many other CMIP6 models E3SMv2 simulates a low surface temperature bias in the middle of 20th century, primarily due to excessive aerosol radiative forcing (Golaz et al., 2022).

Zhang et al. (2022) characterized the aerosol and cloud schemes in the Energy Exascale Earth System Model (E3SM). E3SM represents aerosol processes using the Four-mode Modal Aerosol Module (MAM4), which includes major aerosol species such as sulfate, black carbon, organic matter, dust, sea salt, and marine organic aerosols. MAM4 tracks both interstitial and cloud-borne aerosols across four lognormal modes, assuming internal mixing within each mode and external mixing between modes. Aerosol optical properties are parameterized based on mode radius and refractive index, while water uptake follows Köhler theory with a relative humidity ceiling of 98%.

Cloud droplet activation in E3SM follows the Abdul-Razzak and Ghan (2000) scheme, which determines aerosol activation based on subgrid updraft velocity and aerosol properties such as dry size and hygroscopicity. Instead of using a spectrum of updraft velocities as in previous schemes, E3SMv2 applies a characteristic subgrid updraft velocity, parameterized as a function of turbulent kinetic energy (TKE) from CLUBB. To account for unresolved turbulence effects, including cloud-top radiative cooling, a lower bound of 0.2 m/s—adapted from CAM5.4—is imposed. The activation process is coupled with an explicit vertical diffusion scheme with dynamical sub-stepping, which regulates the vertical transport of aerosols and cloud droplet number concentrations. E3SMv2 enforces a minimum cloud droplet number concentration threshold at 10 cm^{-3} (Golaz et al., 2022).

For mixed-phase clouds, E3SM employs a classical nucleation theory (CNT)-based parameterization, where dust immersion freezing is the dominant mechanism for ice formation (Wang et al., 2014). Cirrus clouds, on the other hand, use the Liu and Penner (2005) scheme to simulate both homogeneous and heterogeneous ice nucleation. Sulfate aerosols in the Aitken mode serve as ice-nucleating particles for homogeneous freezing, with a 50 nm size threshold, which has been tuned to optimize cloud fraction and radiative forcing consistency

2.2 The Volcanic Forcing Representation in E3SMv2

Following the CMIP6 protocol, E3SMv2 employs prescribed volcanic shortwave extinction and longwave absorption above the tropopause (Golaz et al., 2022) (Zanchettin et al., 2016). This CMIP6 stratospheric Aerosol Dataset (SAD) v3 can be found at doi:10.22033/ESGF/input4MIPs.1681 (IACETH, 2017). Particularly, the stratospheric aerosol extinction and absorption are overwritten by prescribed values at each time step. For the period spanning 1979-2014, data predominantly rely on assimilated satellite data from sources like the Stratospheric Aerosol and Gas Experiment (SAGE), SAGEII, the Stratospheric Aerosol Measurement (SAM), the Cloud-Aerosol Lidar and Infrared Pathfinder Satellite Observation (CALIPSO), and the Optical Spectrograph and InfraRed Imager System (OSIRIS), with the Cryogenic Limb Array Etalon Spectrometer (CLAES) data utilized for gap-filling in cases of missing data (Rieger et al., 2020; Thomason et al., 2018). During the period from 1850 to 1978, particularly during volcanically quiescent periods, the monthly mean background aerosol data measured by SAGE II (during the volcanic quiescent period of 1996-2005) is utilized. The volcanic eruption contribution is then calculated using the two-dimensional sulfate aerosol model developed at the Atmospheric and Environmental Research Inc., Lexington, MA, USA (AER-2-D). The AER-2-D model has sulfuric acid aerosol microphysics in a global domain with 9.5° horizontal resolution and 1.2 km vertical resolution. The aerosol microphysics scheme has 40 size bins spanning the range 0.4 nm to 3.2 μm. There is no interaction between aerosols, radiation forcings, and dynamics and the dynamical fields, such as U, V, and T, for all simulated cases are based on Pinatubo eruption climatology (1991). Additionally, stratospheric AOD is calibrated using the photometer data whenever available; otherwise, the best estimate of sulfur ejection is utilized for the volcanic contribution, often estimated from proxies such as ice core data (Arfeuille et al., 2014). For the PI control simulation, the volcanic quiescent background values are used.

173
174 This study focuses on volcanic activities during the year 1940-1979 period (the reason will be described in section
175 2.2). During this period, Arfeuille et al. (2014) recorded two volcanic eruptions (Table 1). For the Agung (1963)
176 eruption, AER-2-D model evenly injected SO_2 in the 15°S-0° and 0°-15°N regions of Southern and Northern
177 Hemispheres, respectively. For the Fuego (1974) eruption, SO_2 was injected evenly in the 0°-15°N band only
178 (Arfeuille et al., 2014). Compared to injecting emissions at limited grids, evenly distributing the emission in a broad
179 latitude band dilutes the SO_2 concentration and consequently results in smaller particle sizes and thus higher
180 efficiency of scattering the solar radiation and prolonged aerosol lifetime (Niemeier et al., 2019; Timmreck et al.,
181 2010).
182
183
184   **2.3 The Interactive Volcanic Sulfate Aerosol Treatment**
185 In E3SMv2, the aerosol process is represented by 4-mode version of the modal aerosol model (MAM4) (Liu et al.,
186 2012; Wang et al., 2019), which is a comprehensive approach to simulate aerosol particles in the Earth system. It
187 encompasses four distinct aerosol modes representing different aerosol types and sizes: Aitken mode, accumulation
188 mode, coarse mode, and primary carbon mode for black carbon and primary organic carbon particles emitted
189 directly into the atmosphere. This model accounts for aerosol processes such as emissions, transport, chemical
190 transformation, and removal.
191
192 In the current version of MAM4, there are six aerosol species represented: sulfate, black carbon, organic carbon,
193 dust, sea salt, and secondary organic aerosols. In E3SMv2, sulfate aerosols primarily originate from the
194 condensation of H_2SO_4 gas as well as aqueous phase production in cloud water. The model utilizes a simple gas-
195 phase chemistry package to calculate the formation of H_2SO_4, incorporating prescribed oxidant, hydroxyl radical
196 (OH), to oxidize SO_2 and DMS gases in the atmosphere.
197
198 It is worth noting that the MAM4 in E3SMv2 hasn't been designed to accurately reproduce the volcanic sulfate
199 aerosol direct effect caused by volcanic eruptions. Modifications are needed to well reproduce the Mt. Pinatubo's
200 (1991) aerosol direct impact on shortwave forcing, compared to observations (Brown et al., 2024; Mills et al., 2016).
201 But such modifications caused unexpected drawbacks of ice cloud formations over upper troposphere and lower
202 stratosphere (Visioni et al., 2017). The remedy efforts for both CESM and E3SM will be represented in a following-
203 up paper that documents a new development of adding a stratospheric sulfate mode on top of MAM4 (Ke et al., in
204 preparation). Furthermore, it is important to use unchanged MAM4 and E3SMv2 configurations to provide an apple-
205 to-apple comparison to evaluate the impacts of the change of volcanic sulfate aerosol representation on simulated
206 aerosol direct and indirect effects during middle of 20th century.
207
208 To introduce interactive volcanic sulfate aerosols into E3SMv2, we utilize the volcanic Emissions from Earth
209 System Models (volcanEESM) dataset, which serves as a source of volcanic SO_2 emissions (Danabasoglu et al.,
210 2020; Neely and Schmidt, 2016). This dataset, funded by the NCAR/UCAR Atmospheric Chemistry and Modeling
211 Visiting Scientist Program and the University of Leeds School of Earth and Environment, provides detailed
212 information on historical volcanic eruptions, including dates, locations, injection height ranges, and SO_2 emission
213 amounts. Given that E3SMv2 lacks comprehensive stratospheric chemistry for processing SO_2 gas, we employ the
214 simplified chemistry package where volcanic SO_2 is oxidized using prescribed OH concentrations derived from the
215 historical monthly mean from the CESM-WACCM simulations. Past research has demonstrated that this approach
216 yields reasonable results with high efficiency compared to models employing the comprehensive stratospheric
217 chemistry (Smith et al., 2014). We validate this approach by comparing the simulated interactive stratospheric
218 aerosol optical depth (SAOD) in E3SMv2 with SAOD produced using the default method (see Figure 2).
219
220 Figure 2 depicts the simulated SAOD based on volcanEESM dataset and CMIP6 default method, respectively.
221 Generally, the two simulated SAOD curves align closely in terms of eruption timing and intensity. However, notable
222 discrepancies emerge between 1940 and 1980 (black dashed box). Specifically, volcanEESM records two moderate-
223 intensity eruptions during 1940 to 1950, whereas no eruptions are recorded in the CMIP6 volcanic dataset for this
224 period. Additionally, the CMIP6 shows higher SAOD values than those predicted from the volcanEESM for the Mt.
225 Agung (1963) eruption and the two subsequent eruptions, which were not recorded in the CMIP6 document (Table
226 1, Arfeuille et al., 2014). These significant disparities motivate our study to investigate the impact of the
227 volcanEESM inventory on simulated climate compared to that using the default E3SMv2 model with the CMIP6
228 volcanic dataset. The volcanic eruptions during 1940 to 1980 from CMIP6 and volcanEESM are presented in Tables

229 1 and 2, respectively. Table 2 lists the recorded explosive eruptions from the volcanEESM dataset for the period
230 1940–1979. In Section 3.1, we compare the simulated Agung eruption with results from other studies, demonstrating
231 that the new approach better captures volcanic sulfate aerosol-radiation interactions in terms of both magnitude and
232 spatial distribution than the CMIP6 prescribed stratospheric forcing. This comparison supports the validity of the
233 emission-based approach in improving the representation of volcanic aerosol forcing

235 In summary, during the SAGE period, the original method (prescribed stratospheric forcing) incorporates observed
236 aerosol extinctions, which likely provides a more accurate representation of stratospheric aerosol-radiation
237 interactions compared to the SO2-emission-based approach—assuming that stratospheric aerosol sedimentation into
238 the troposphere does not significantly affect radiative forcing. However, for the mid-century period, both methods
239 rely on SO2 emission estimates, which are inherently uncertain. The key improvements in our approach stem from
240 (1) the inclusion of updated explosive SO2 injection events, ensuring a more physically consistent representation of
241 volcanic forcing, and (2) the incorporation of aerosol-cloud interactions through the cloud condensation nuclei
242 (CCN) effect from volcanic sulfate aerosols, which was absent in the original approach.
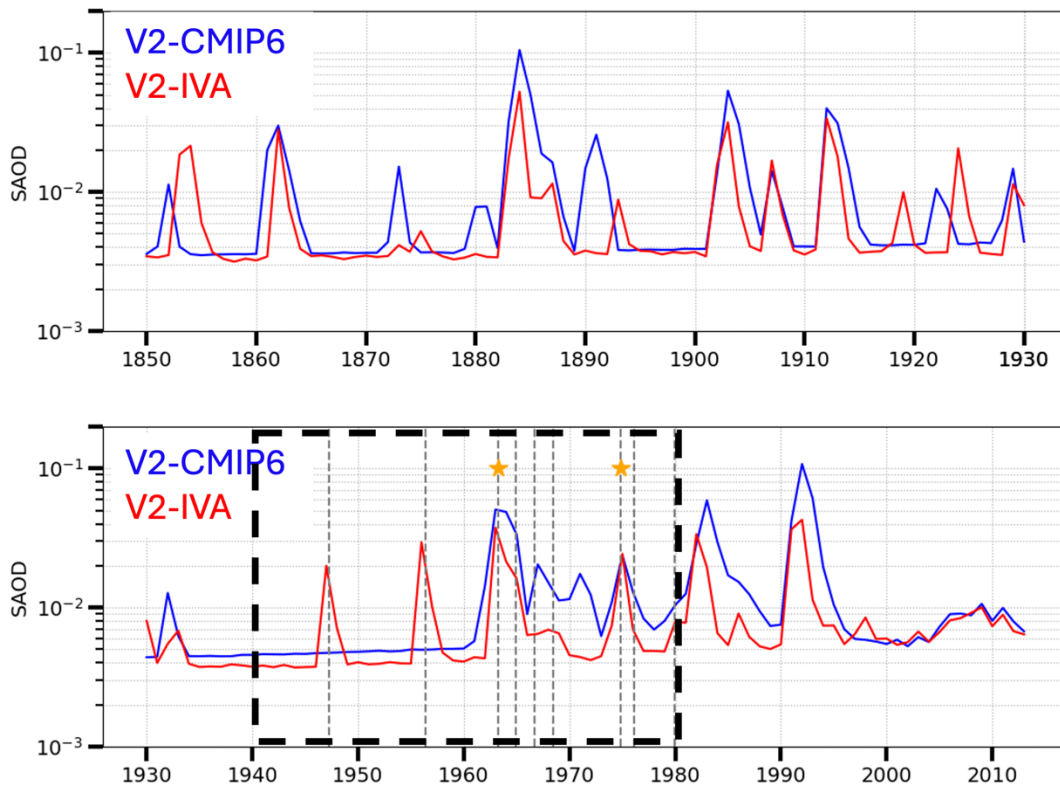
246 Figure 2. The simulated stratospheric AOD (SAOD) by E3SMv2 using different volcanic representations. The
247 E3SMv2 with CMIP6 prescribed volcanic scattering (V2-CMIP6) is shown in blue line, while the E3SMv2 with
248 interactive volcanic sulfate aerosol treatment (V2-IVA) is shown in red line. During the year 1940-1980 period, the
249 volcanic eruptions recorded by CMIP6 data are marked by orange stars, while the eruptions recorded by
250 volcanEESM are marked by grey dashed lines.

256 Table 1. Recorded explosive eruptions based on Arfeuille2014 (CMIP6).

	Injection Height (km)	NH (SO2 Tg)	SH (SO2 Tg)
1963 Agung	27	3.4	6.5
1974 Fuego	33.5 (as Pinatubo)	2.3	0.0

Table 2. Recorded explosive eruptions from volcanEESM during year 1940-1979.

YYYY/MM/DD	LAT	LON	ALTMIN	ALTMAX	SO2(TG)
1947/03/29	64.0	339.3	15.0	19.6	2.3
1956/03/30	56.0	160.6	15.5	18.5	3.9
1963/03/17	-8.3	115.5	18.0	20.0	7.5
1964/11/12	56.7	161.4	15.0	19.6	2.3
1966/08/12	3.7	125.5	15.0	19.6	0.8
1968/06/11	-0.4	267.5	15.0	19.6	0.8
1974/10/10	14.5	268.1	16.7	21.3	3.0
1976/01/22	59.4	205.6	7.0	10.0	0.8
1979/11/13	-0.8	268.8	1.5	14.0	1.2

295
296
297
298
299
300
301
302
303
304   **2.4 The Experimental Design**
305 2.4.1 **Averaged volcanic emission in pre-industrial control simulation**
306 The CMIP6 protocol recommends using averaged volcanic forcing in the historical period in the PI control
307 simulations. The average volcanic SO_2 emission is 2.26×10^{-8} Tg s^{-1}, equivalent to 0.7 Tg year^{-1}, calculated by
308 averaging emissions from all eruptions between 1850 and 2014. To determine the horizontal emission distribution,
309 we assume a normal distribution along latitude and even distribution along longitude. Using each eruption amount as
310 a weight, the weighted mean emission latitude is 20.67º north, with a standard deviation of 28.83º. Vertically, the
311 mean injection height has an upper limit of 18 km and a lower limit of 14 km. The impact of PI control aerosols on
312 simulated transient climate has been discussed in supplement materials (Text S1 and Table S1).
313

314 2.4.2 **Simulation Design**
315 The V2-CMIP6 (control) run comprises a 5-member ensemble of E3SMv2 coupled historical transient simulations
316 spanning from 1850 to 2014, conducted and archived by Golaz et al., 2022. In contrast, the V2-IVA experiment
317 investigates the influence of interactive volcanic sulfate aerosols on historical transient simulations by replacing the
318 default prescribed volcanic stratospheric forcing with volcanic SO_2 emissions in E3SMv2. This experiment
319 underwent a 100-year spin-up under the same preindustrial (PI) control configuration as V2-CMIP6, except with
320 interactive volcanic treatment, utilizing averaged volcanic emissions from 1850 to 2014 (see section 2.4.1).
321 Following the model spin-up, one member simulation is conducted from 1850 to 2014, with additional two members
322 conducted from 1940 to 2014 to minimize noise in coupled simulations. By comparing V2-IVA to V2-CMIP6, the
323 impact of volcanic treatments on simulated climate can be assessed.
324
325
326
327 **Table 3**. Experiment configurations.

	Simulation Type	Historical Volcanic Forcing	piControl Volcanic Setting
V2-CMIP6 (E3SMv2 default)	V2 archived 5 members: 1850-2014	Prescribed in Stratosphere (following CMIP6)	Prescribed in Stratosphere (volcanic quiescent background)
V2-IVA	1 member 1850-1940 3 members 1940-2014	Interactive treatment (using VolcanEESM)	Averaged emission (1850-2014)

328
329
330
331
332
333 **3.   Results**
334 **3.1 Simulated Sulfate Aerosols**
335 VolcanEESM recorded eight eruptions during the years spanning 1940-1979 (see Table 2). These eruptions are
336 directly reflected in sulfate aerosol concentrations simulated by the V2-IVA experiment (see Figure 3, panel a).
337 Prior to these eruptions, the background sulfate aerosol concentration between 100 and 50 hPa was approximately
338 0.1 μg/kg. Hekla (1947) and Bezymianny (1956), emitting 2.3 and 3.9 Tg SO_2 gas respectively, induced spikes in
339 sulfate aerosol concentrations, with global mean concentration peaks reaching up to 7 and 12 μg/kg in the
340 stratosphere, respectively. The eruption of Mt. Agung in 1963 with a SO_2 emission of 7.5 Tg, caused a peak global
341 mean concentration of up to 20 μg/kg between 100 and 10 hPa. Subsequent to the Mt. Agung (1963) eruption, three
342 eruptions resulted in high aerosol concentrations lingering in the stratosphere until 1972, with eruptions in 1974 and
343 1976 sustaining global mean concentrations above 0.5 μg/kg for additional four years.
344

345 In addition to their significant amounts in the stratosphere, volcanic sulfate aerosols gradually descended into the
346 troposphere. As V2-CMIP6 did not account for volcanic sulfate aerosols, the sulfate aerosol difference between V2-
347 IVA and V2-CMIP6 illustrates the descent of these aerosols into the troposphere, which is depicted in Figures 4b to
348 4e. Four out of the eight eruptions recorded by volcanEESM (1947, 1956, 1964, 1976) occurred in northern
349 hemisphere high latitudes (above 50° N), while the other four occurred in the tropical regions (20° S to 20° N, see
350 Table 2). Strong sulfate aerosol footprints were observed in the troposphere (below the tropopause, gray lines) in
351 northern high latitudes (Figure 3c) compared to tropics (Figure 3d) and southern high latitudes (Figure 3e). Despite
352 no eruptions occurring in southern hemisphere high latitudes, volcanic sulfate aerosols tended to descend more over
353 these regions compared to tropical regions due to the Brewer-Dobson circulation. Overall, a substantial amount of
354 sulfate aerosols reached the troposphere from the stratosphere, highlighting the potential aerosol-cloud interactions.
355
356 SAOD describes the impact of aerosols on the optical properties of the atmosphere in the stratosphere. The
357 simulated SAOD from the V2-IVA ensemble is shown in Figure 4, upper panel. Prior to eruptions, the background
358 SAOD values were approximately 0.008 over high latitudes and 0.002 over the tropics. The volcanic eruptions of
359 Hekla (1947) and Bezymianny (1956) elevated SAOD to 0.06 and 0.13 over northern hemisphere high latitudes
360 (compared to Figure 4 in Danabasoglu et al., 2020). Since these two volcanic eruptions were absent in V2-CMIP6,
361 the two red spikes emerged when comparing V2-IVA with V2-CMIP6 (Figure 4 lower panel). Despite their
362 relatively small magnitudes, the impact of these two volcanoes was limited to two years and north of 30 degrees in
363 the Northern Hemisphere.
364
365 For the Mt. Agung eruption in 1963, V2-IVA SAOD displayed a clear spike spreading from the tropics to the South
366 Pole, with peak values exceeding 0.2, consistent with previous studies (Dhomse et al., 2020; Niemeier et al., 2019) .
367 Due to a lower strength recorded by volcanEESM, the simulated SAOD in V2-IVA was approximately 0.03 lower
368 than in V2-CMIP6 (Figure 4, lower panel). Additionally, V2-CMIP6 simulation indicated three events with slightly
369 higher SAOD than V2-IVA in 1967, 1972, and 1974, spanning from the tropics to southern hemisphere high
370 latitudes, while V2-IVA recorded an extra eruption in 1976 in northern hemisphere high latitudes. Consequently,
371 V2-IVA simulated two moderate volcanic eruptions during the 1940-1959 period and a relatively dimmer volcanic
372 impact over the 1960-1979 period.
373
374 Aerosol extinction vertical profiles measure the scattering and absorption of solar radiation by aerosols. Figure 5
375 examines the difference in simulated extinction between V2-IVA and V2-CMIP6 across time and pressure levels. In
376 the V2-IVA simulation, extinction resulted from simulated aerosol scattering and absorption effects, including
377 volcanic sulfate aerosols, whereas in V2-CMIP6, the extinction caused by volcanic eruptions was prescribed. In the
378 panel for global mean, distinct red stripes caused by the Hekla (1947) and Bezymianny (1956) eruptions extend
379 from the stratosphere into the upper troposphere, coinciding with the comparison of sulfate aerosol concentrations
380 (Figure 3). This is attributed to V2-IVA's interactive treatment of volcanic sulfate aerosols, allowing for their
381 aerosols extinction effect to penetrate below the stratosphere as particles descend into the troposphere, a more
382 realistic representation compared to the prescribed treatment in V2-CMIP6. The aerosols extinction of the Hekla
383 (1947) and Bezymianny (1956) eruptions is primarily observed between 50 and 350 hPa globally. In northern high
384 latitudes, the impact of the Bezymianny (1956) eruption could extend to the middle to lower troposphere below 500
385 hPa, whereas its impact over the tropics was relatively weaker.
386
387 Regarding the Mt. Agung eruption, V2-IVA simulated a weaker extinction above 100 hPa compared to V2-CMIP6,
388 resulting in negative values. However, V2-IVA simulated stronger extinction between 100 and 300 hPa compared to
389 V2-CMIP6, as the injection was concentrated in the middle to lower stratosphere (18-20 km) in V2-IVA (see Table
390 2). For the eruptions subsequent to Mt. Agung, V2-IVA simulated weaker eruptions compared to V2-CMIP6 on a
391 global average. In detail, V2-IVA simulated slightly stronger extinctions over northern high latitudes, while showing
392 reduced scattering over the tropics and the southern hemisphere.
393
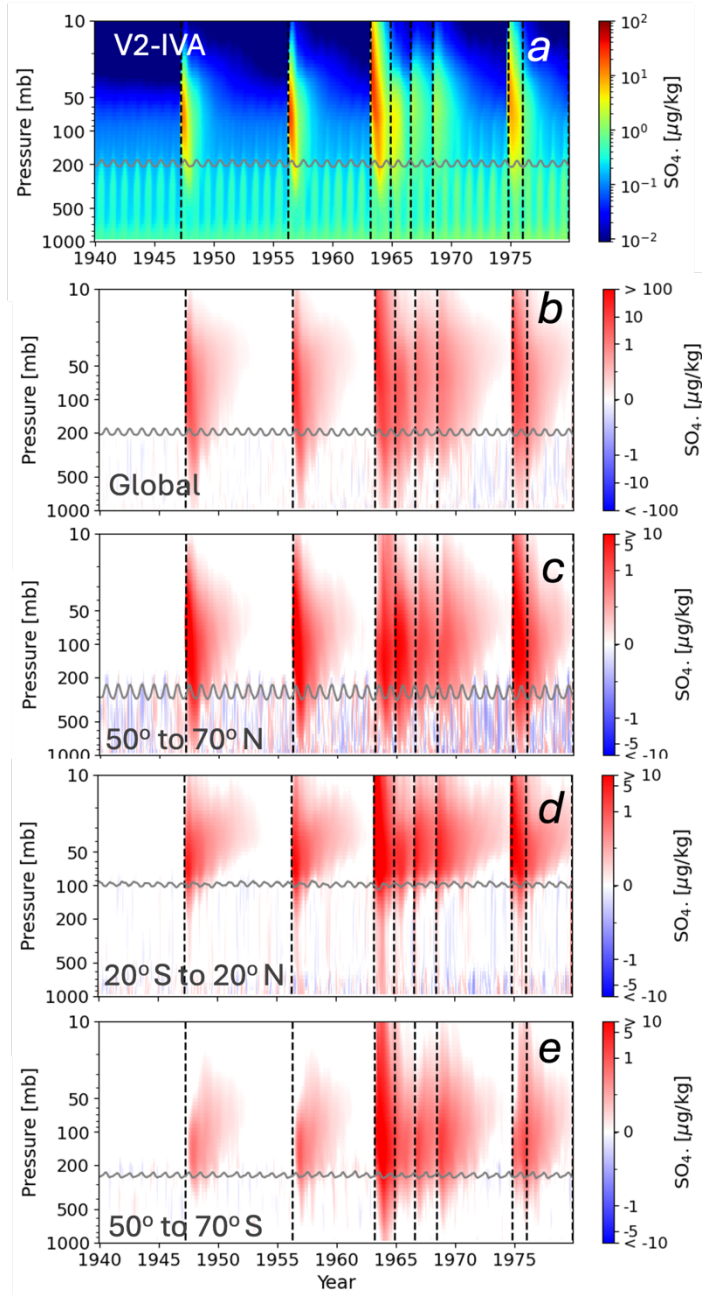
Figure 3. Simulated sulfate (SO4) aerosol concentrations or differences (μg/kg). The x-axis represents time in years, while y-axis represents pressure levels in hPa. The global averaged sulfate aerosol concentrations from V2-IVA are shown in panel *a*. Panels b-e show the SO4 concentration differences between experiment V2-IVA and V2-CMIP6 over different latitude bands. The eruptions recorded by volcanEESM are marked by grey dashed lines (see Table 2).
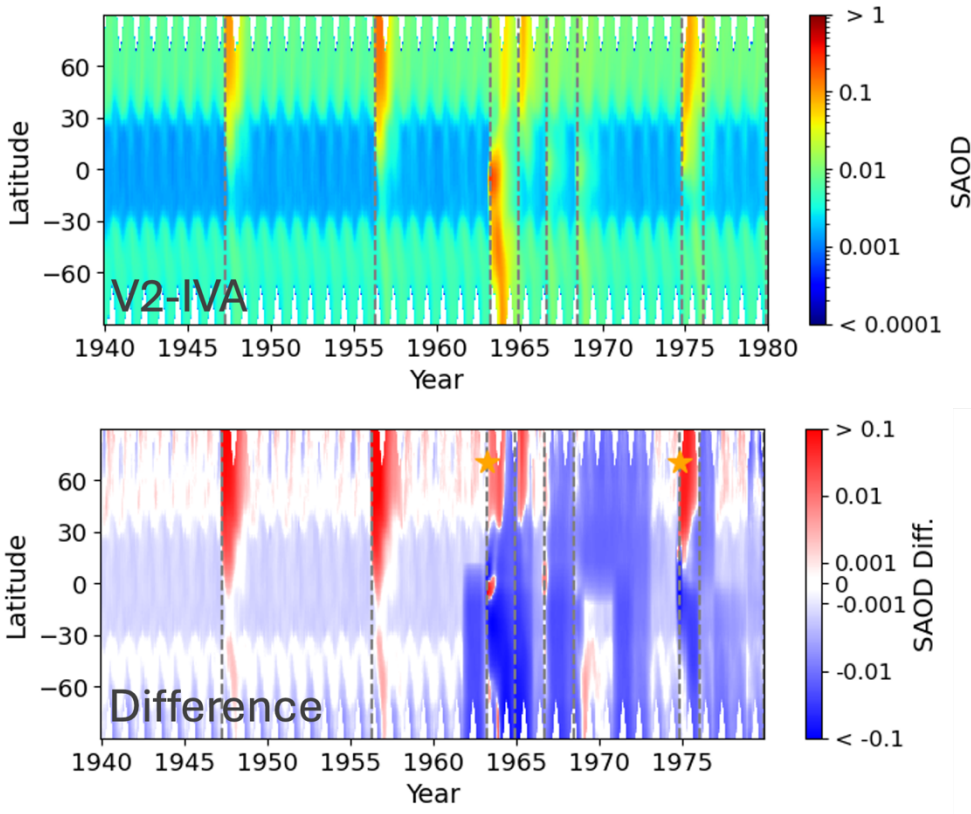
Figure 4. Simulated time (in year) and latitude (in degree) variations of SAOD from V2-IVA ensemble (upper panel) and the SAOD difference between V2-IVA and V2-CMIP6 (bottom panel). The dashed lines represent volcanic eruptions in volcanEESM (Table 2), while the stars indicate volcanic eruptions in the CMIP6 documentation (Table 1)
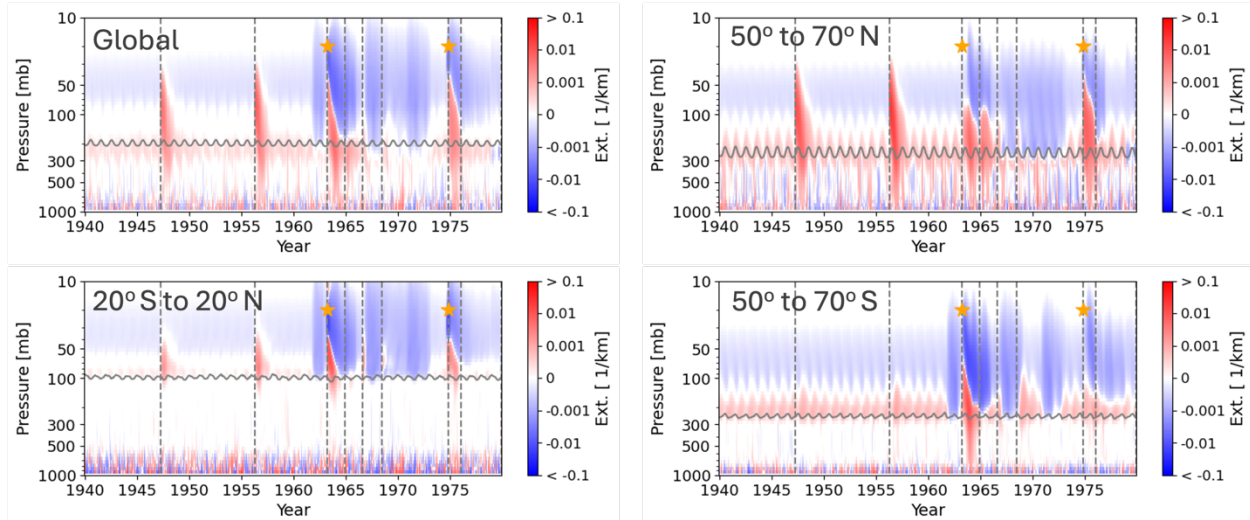
Figure 5. Difference of mean extinction between V2-IVA and V2-CMIP6 over the entire globe and at different latitude bands. The x-axis represents time in years, and the y-axis represents pressure level in hPa. The vertical dashed lines represent volcanic eruptions in volcanEESM (Table 2), while the stars indicate volcanic eruptions in the CMIP6 documentation (Table 1). The solid gray curves represent tropopause simulated by model.

3.2 Simulated Radiative Forcings

Figure 6 presents the radiative forcing anomalies from the V2-IVA and V2-CMIP6 ensembles, calculated as deviations from the corresponding 1850–1900 climatological mean. These anomalies provide insight into how volcanic eruptions influenced the radiative budget during the 1940–1980 period.

Panel a shows the shortwave radiative forcing anomaly at the top of the atmosphere (TOA) under clear-sky conditions, which primarily reflects the direct radiative effect of volcanic sulfate aerosols. As expected, the 1947 Hekla and 1956 Bezymianny eruptions caused clear-sky cooling effects in the V2-IVA simulations, with global mean radiative forcing drops of approximately 1.2 W/m² and 2.3 W/m², respectively. These signals persisted for several months before recovering, while no such effects were observed in the V2-CMIP6 simulations. The 1963 Mt. Agung eruption led to a 3.7 W/m² decrease in shortwave radiative forcing in V2-IVA, compared to a 4.3 W/m² drop in V2-CMIP6. By 1966, both simulations showed similar forcing levels, with slight discrepancies appearing in subsequent years due to differences in volcanic forcing representation. The relatively weaker initial forcing in V2-IVA is consistent with prior studies suggesting that the CMIP6 prescribed stratospheric forcing for Mt. Agung may be overestimated (Chylek et al., 2020; Dhomse et al., 2020; Niemeier et al., 2019). These results demonstrate that the emission-based approach in V2-IVA provides a reasonable representation of volcanic sulfate aerosol-radiation interactions (VARIs), capturing the expected radiative response to major eruptions.

Figure 6c presents the cloud radiative forcing anomaly at TOA, which is critical for understanding the role of volcanic sulfate aerosols in modifying cloud properties. The V2-IVA and V2-CMIP6 simulations exhibit distinct cloud forcing responses due to their respective volcanic aerosol treatments. During the 1940–1959 period, the V2-IVA ensemble mean anomaly is -0.61 W/m², which is 0.11 W/m² higher (less cooling) than the V2-CMIP6 mean anomaly of -0.72 W/m². This difference is statistically significant at the 95% confidence level. In the 1960–1980 period, the V2-IVA ensemble mean anomaly is -0.98 W/m², compared to -0.91 W/m² in V2-CMIP6, indicating a stronger cooling effect in V2-IVA by -0.07 W/m², which is also statistically significant. The V2-CMIP6 cloud forcing values are in line with Golaz et al. (2022) and comparable to values from other models during the similar period (Bauer et al., 2020; Flynn and Mauritsen, 2020; Zhang et al., 2021), which contributes to the simulated surface temperature low bias by E3SMv2 (Golaz et al., 2022).

457 These differences in cloud forcing anomalies between two ensembles align with expectations based on the inclusion
458 of volcanic sulfate aerosols in the pre-industrial (PI) background in V2-IVA. As discussed in the introduction,
459 incorporating historical average volcanic sulfate emissions into PI control simulations alters the baseline for aerosol-
460 cloud interactions, $\frac{A_a + A_v}{A_{PI} + \overline{A_v}}$, (equation 2). During the 1940–1959 period, characterized by relatively low volcanic
461 activity, the low volcanic sulfate aerosols (A_v) in V2-IVA with large baseline aerosols ($A_{PI} + \overline{A_v}$) and the same other
462 aerosol increase (A_a) resulted in lower aerosol relative increase (R_v) compared to V2-CMIP6 aerosol increase ration
463 $\frac{A_a}{A_{PI}}$ during the same period. In contrast, the 1960–1980 period, marked by more frequent and intense volcanic
464 eruptions, saw additional sulfate aerosols injected into the atmosphere, indicating larger A_v, enhancing aerosol-cloud
465 interactions and leading to stronger cloud cooling in V2-IVA. This effect is evident in the lower (more negative)
466 cloud forcing anomaly compared to the 1940–1960 period, confirming that volcanic sulfate aerosol variability plays
467 a crucial role in modulating cloud radiative effects.
468
469 Panel b shows the net radiative forcing anomaly at TOA, which integrates both shortwave and longwave
470 contributions. The Mt. Agung eruption in 1963 is the only event in the 1940–1980 period that produces a clear
471 negative forcing signal. The V2-CMIP6 simulation exhibits a maximum radiative forcing drop of 3.5 W/m², which
472 takes approximately three years to recover, while V2-IVA simulates a smaller initial drop of 2.5 W/m². Apart from
473 Mt. Agung, no significant changes in TOA net radiative forcing are evident for other volcanic events, highlighting
474 the dominance of anthropogenic aerosol trends in shaping the overall radiative balance during this period.
475
476
477
478
479
480
481
482
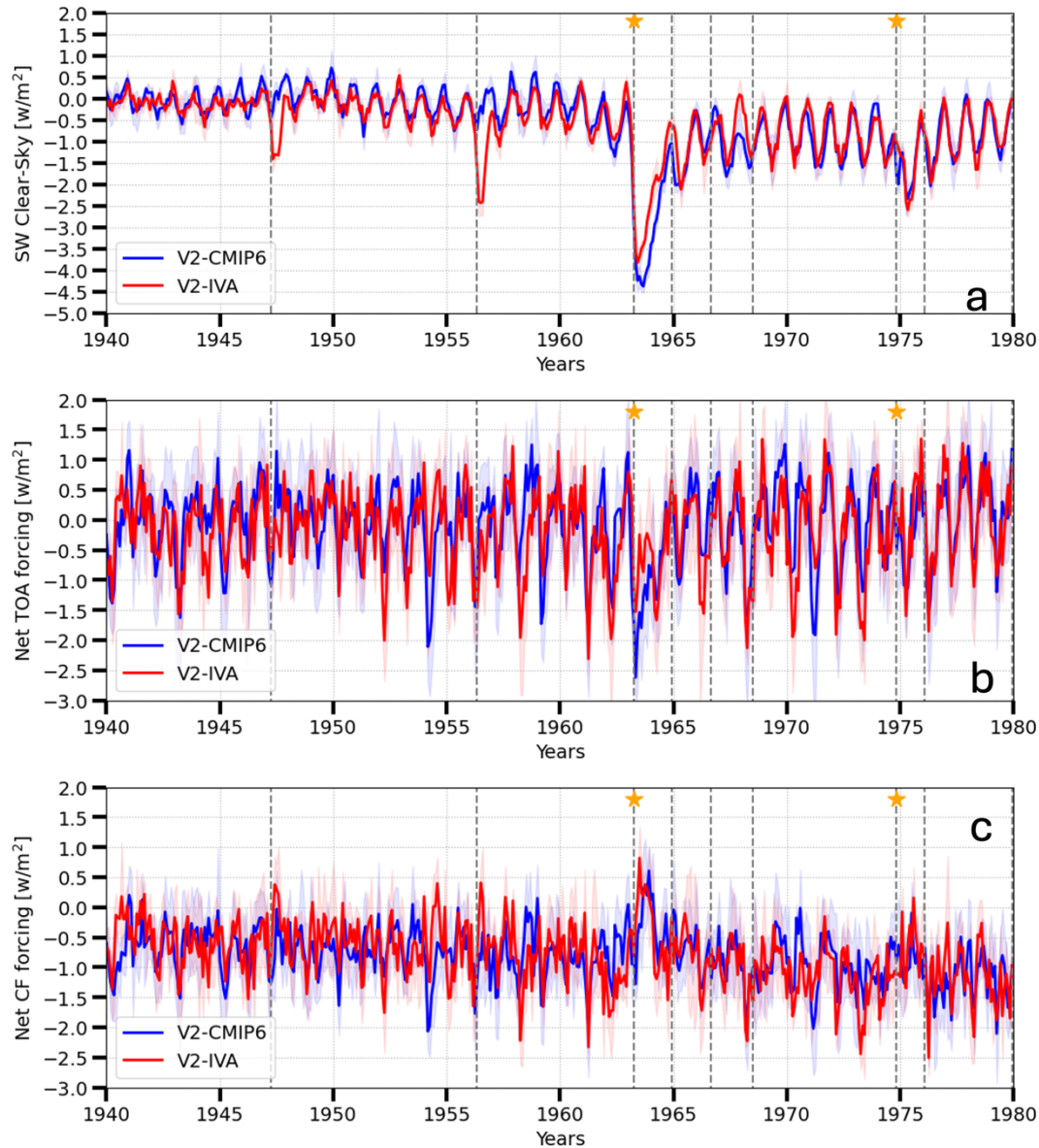
Figure 6. Time series of simulated global mean radiative forcings anomalies by V2-IVA and V2-CMIP6 ensembles, including the clear-sky shortwave forcing (*a*), net forcing at TOA (*b*), and net cloud forcing at TOA (*c*). The ensemble mean of forcings are shown as solid lines, with the one-standard-deviation range represented as color shading to indicate uncertainty. The vertical dashed lines represent volcanic eruptions in volcanEESM (Table 2), while the stars indicate volcanic eruptions in the CMIP6 documentation (Table 1).

3.3 Simulated Cloud Changes with Volcanic Activities

This section examines cloud property changes over time to support the cloud forcing differences discussed in Section 3.2. The difference in net cloud forcing anomalies between the V2-IVA and V2-CMIP6 ensembles is 0.11 W/m² (warming effect) for the 1940–1959 period and -0.08 W/m² (cooling effect) for the 1960–1979 period. These changes align with variations in volcanic activity levels during these periods, with relatively low volcanic emissions in 1940–1959 and elevated emissions in 1960–1979. The shortwave cloud forcing exhibits a similar pattern (Table 4).

501 In the V2-IVA experiment, volcanic sulfate aerosols (A_v) actively participate in aerosol-cloud interactions,
502 modifying cloud properties in response to fluctuations in volcanic emissions. During 1940–1959, the volcanEESM
503 inventory recorded two moderate eruptions, Hekla (1947) and Bezymianny (1956), contributing a total of 6.2 Tg
504 SO_2 emissions, or an average of 3.1 Tg per decade. This is lower than both the historical average (7.0 Tg per decade)
505 and the 1850–1899 climatology (6.5 Tg per decade), indicating a reduction in volcanic sulfate emissions during this
506 period. Since the total aerosol burden in the atmosphere is determined by both historical aerosols increase (A_a) and
507 volcanic aerosols (A_v), a lower A_v value in this period partially compensates the A_a increase and lowers aerosol
508 increase ratio R_v (equation 2) compared to V2-CMIP6 experiment. This lower R_v results in relative lower cloud
509 droplet number concentration (CDNC), cloud cover, and cloud liquid water content leading to weaker aerosol-cloud
510 interactions in the historical transient simulation (Figure 7, left column). These reductions occur relatively uniformly
511 across latitudes rather than being concentrated in specific regions.

512 In contrast, the 1960–1979 period experienced significantly higher volcanic SO_2 emissions, totaling 16.4 Tg, or 8.2
513 Tg per decade (Table 2), which exceeds the 1850–1899 climatology of 6.5 Tg per decade. The larger A_v value
514 during this period lowers the R_v ratio, meaning that volcanic aerosols contribute more to the total aerosol burden, as
515 well as other aerosol increase. The increase in volcanic sulfate aerosols results in a 28% increase in low cloud
516 fraction anomaly, a 5% increase in cloud liquid water path anomaly, and a 1% increase in vertically integrated
517 CDNC in V2-IVA compared to V2-CMIP6 (Figure 7. right column and Table 4). These cloud property changes
518 support a cooling effect on net cloud forcing of -0.08 W/m². The simulated cloud fraction anomaly values are
519 reasonable and in line with the study that evaluates CMIP6 cloud fraction variations across different climate models
520 (Vignesh et al., 2020).
521
522
523
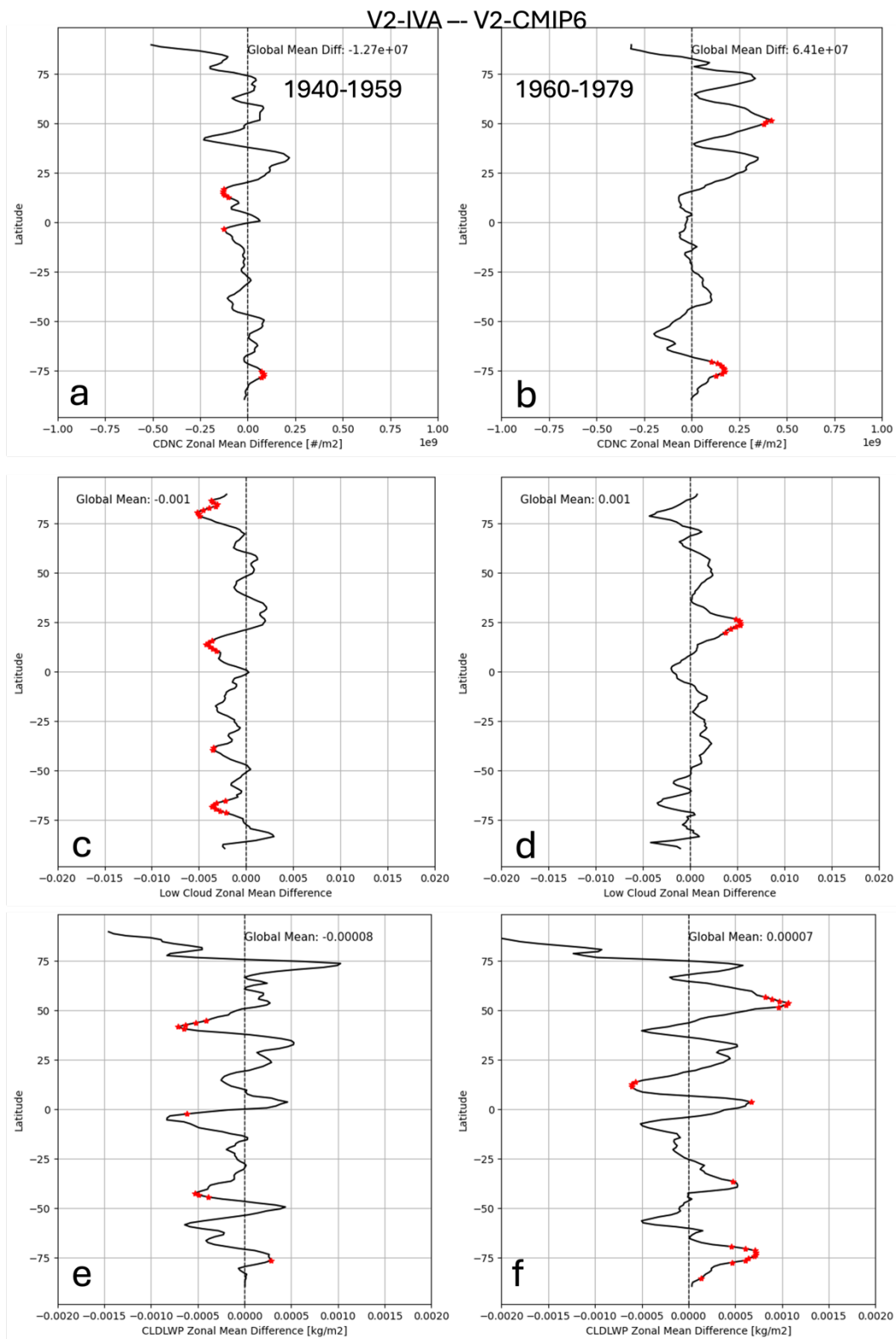
524
525
526 Figure 7. Simulated difference in cloud property anomalies between V2-IVA and V2-CMIP6 ensembles for 1940-
527 1959 period (left column) and 1960-1979 period (right column). The comparison includes (top row) zonal mean
528 vertical integrated cloud droplet number concentration (CDNC) in units of #/m², (middle row) low cloud cover, and

 (bottom row) cloud liquid water path (LWP) in units of kg/m2. The y-axis in each panel represents latitude
530 (degree).The red dotted points represent the difference are significant at 95% confidence level.
531
532
533
534
535
536 Table 4. Differences in global mean cloud property anomalies between V2-IVA and V2-CMIP6. The numbers in the
537 brackets are anomalies resulted from V2-IVA and V2-CMIP6 ensembles, respectively. Values with * represent
538 statistically significant at the 95% confidence level.
539

Anomaly Difference	1940-1959	1960-1979
Net Cloud Forcing (W/m^2)	0.11* (-0.61, -0.72)	-0.07* (-0.98, -0.91)
SW Cloud Forcing (W/m^2)	0.16* (-0.50, -0.65)	-0.04 (-0.78, -0.74)
Vertically-integrated CDNC (#/m2)	-1.27×10^7 (2.46×10^9, 2.48×10^9)	6.41×10^7 (4.44×10^9, 4.37×10^9)
Total Cloud Fraction	-1.46×10^{-3}* (1.37×10^{-3}, 2.83×10^{-3})	-0.01×10^{-3} (3.06×10^{-3}, 3.11×10^{-3})
Low Cloud Fraction	-1.13×10^{-3}* (1.31×10^{-3}, 2.44×10^{-3})	0.81×10^{-3} (3.69×10^{-3}, 2.89×10^{-3})
High Cloud Fraction	-1.09×10^{-3}* (-0.09×10^{-3}, 1.00×10^{-3})	-0.61×10^{-3} (-0.56×10^{-3}, 0.03×10^{-3})
Cloud Liquid Water Path (kg/m^2)	-0.07×10^{-3} (0.97×10^{-3}, 1.05×10^{-3})	0.05×10^{-3} (1.48×10^{-3}, 1.41×10^{-3})
Cloud Ice Water Path (kg/m2)	-0.05×10^{-4} (-1.13×10^{-4}, -1.08×10^{-4})	-0.45×10^{-4} (-1.37×10^{-4}, -0.92×10^{-4})

540
541
542
543
544 **3.4 Simulated Historical Temperature**
545 Since each historical experiment began with a different baseline derived from distinct PI control simulations,
546 directly comparing simulated temperatures across ensembles is not meaningful. Instead, it is more appropriate to
547 compare temperature anomalies from ensemble means, which represent temperature departures from its 1850-1899
548 climatology. For instance, the temperature anomaly for V2-CMIP6 during the 1940-1979 period was calculated by
549 V2-CMIP6 ensemble mean temperature during year 1940-1979 period subtracting the V2-CMIP6 ensemble
550 climatology during the 1850-1899 period. This approach intends to evaluate the changes relative to the climate
551 before anthropogenic emissions took off.
552
553 Figure 8 illustrates the difference in temperature anomalies between V2-IVA and V2-CMIP6. During the 1940-1959
554 period, the eruptions of Hekla (1947) and Bezymianny (1956) lead to brief stratospheric warming. However, V2-
555 IVA shows cooler temperatures in the troposphere shortly after these eruptions compared to V2-CMIP6, particularly
556 over northern high latitudes. This contrast becomes more pronounced when examining temperature anomalies at
557 different pressure levels in Figure 9. At the 200 hPa level, V2-IVA exhibites higher temperature anomalies than V2-
558 CMIP6 after these two eruptions, whereas the situation has been reversed at 500 hPa and the surface. Notably,
559 eruptions only cause short-lived cooling in the troposphere. In general, V2-IVA simulated a warmer troposphere
560 than V2-CMIP6 during the 1940-1959 period.
561
562 During the 1963-1972 period, updated volcanic eruptions resulte in a cooler middle to upper stratosphere in V2-IVA
563 due to reduced aerosol absorption (Figure 5). Consequently, temperatures at 200 hPa level to the surface are
564 moderately warmer in the V2-IVA ensemble compared to the V2-CMIP6 ensemble. Figure 9 shows that V2-IVA
565 simulated temperature anomalies are greater than V2-CMIP6 simulated ones at all three levels. By 1968, the

566   temperature difference between V2-IVA and V2 reaches 0.16 °C at the surface, 0.21 °C at 500 hPa, and 0.22 °C at
567   200 hPa. These findings highlight how differences in the volcanic representation impact interannual temperature
568   changes. In general, V2-IVA simulates a slightly warmer troposphere than that simulated by V2-CMIP6 during the
569   1960-1979 period mainly due to warmer clear-sky shortwave forcing, 0.13 W/m^2, resulted from less volcanic sulfate
570   aerosol radiation interaction from volcanic eruptions, which agree with previous studies (Chylek et al., 2020).
571   Previous studies ((Dhomse et al., 2020; Niemeier et al., 2019) indicated that the smaller
572   Mt Agung (1963) emission, around 7 Tg SO$_2$, should be used in climate models compared to the 9.9 Tg SO$_2$ used in
573   CMIP6 volcanic forcing simulation (Arfeuille et al., 2014).
574
575   Figure 10 presents the simulated surface temperature anomalies compared to observations, with three observational
576   datasets shown as solid gray to black lines. We select the HadCRUT5-Analysis product (Morice et al., 2021),
577   NOAA's National Climatic Data Center (NCDC) NCEP reanalysis dateset, and NASA Goddard Institute Surface
578   Temperature (GISTEMP) dateset (Hansen et al. 2010). Between 1940 and 1959, observations exhibit interannual
579   variability of up to 0.25°C, along with a moderate cooling trend. In contrast, V2-CMIP6 produces a nearly flat
580   temperature curve during this period. V2-IVA improves the interannual variability by incorporating two additional
581   volcanic eruptions, Hekla (1947) and Bezymianny (1956), which introduce episodic cooling events. As a result, the
582   correlation coefficient between the simulated and observed temperature anomalies increases from 0.15 in V2-
583   CMIP6 to 0.38 in V2-IVA, suggesting an improved representation of temperature temporal variability. However, the
584   mean surface temperature anomaly simulated by V2-IVA is only slightly warmer (by 0.02°C) than that of V2-
585   CMIP6, indicating that the main cold bias remains largely unchanged.
586
587   Between 1960 and 1979, the observations show a moderate temperature drop (up to 0.3°C) following the Mt. Agung
588   eruption, but temperatures quickly recover to pre-eruption levels in the early 1970s, with an overall weak warming
589   trend. In contrast, while V2-IVA simulates a slightly warmer temperature anomaly after Mt. Agung compared to
590   V2-CMIP6, the model does not capture the observed temperature rebound. Instead, both simulations exhibit a
591   continued cooling trend over this two-decade period. This result suggests that while the revised volcanic forcing in
592   V2-IVA slightly moderates the excessive cooling seen in V2-CMIP6, it does not clearly correct the underlying bias,
593   indicating that additional factors beyond volcanic forcing may contribute to the mid-20th-century temperature
594   discrepancies.
595
596
597
598
599
600
601
602
603
604
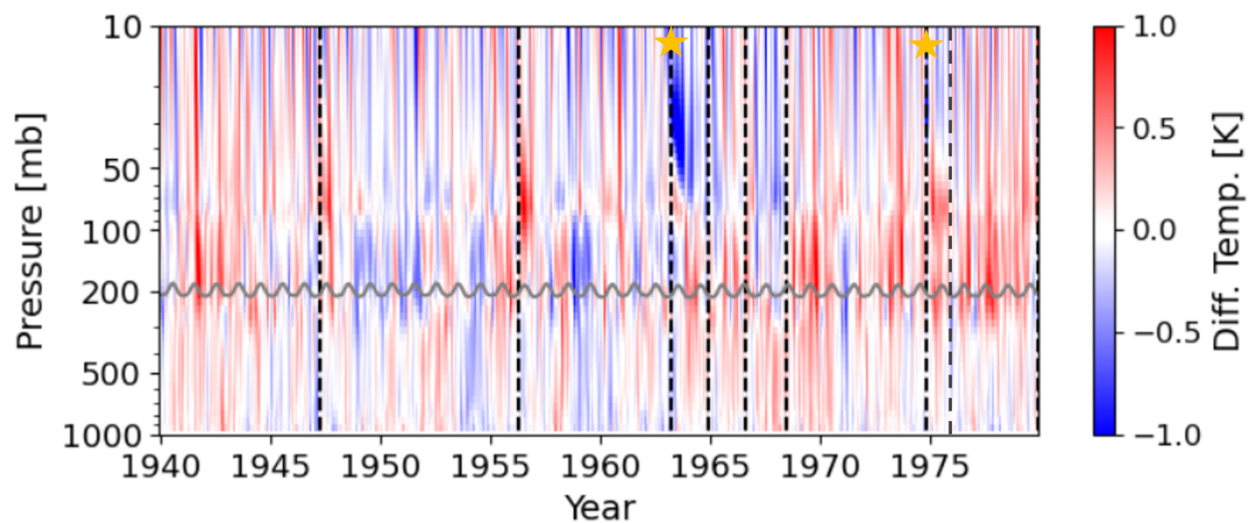
Figure 8. Time-pressure cross-section of global mean temperature difference (K) between V2-IVA and V2-CMIP6 ensembles. The vertical dashed lines represent volcanic eruptions in volcanEESM (Table 2), while the stars indicate volcanic eruptions in the CMIP6 documentation (Table 1). The solid gray curves represent tropopause simulated by model.
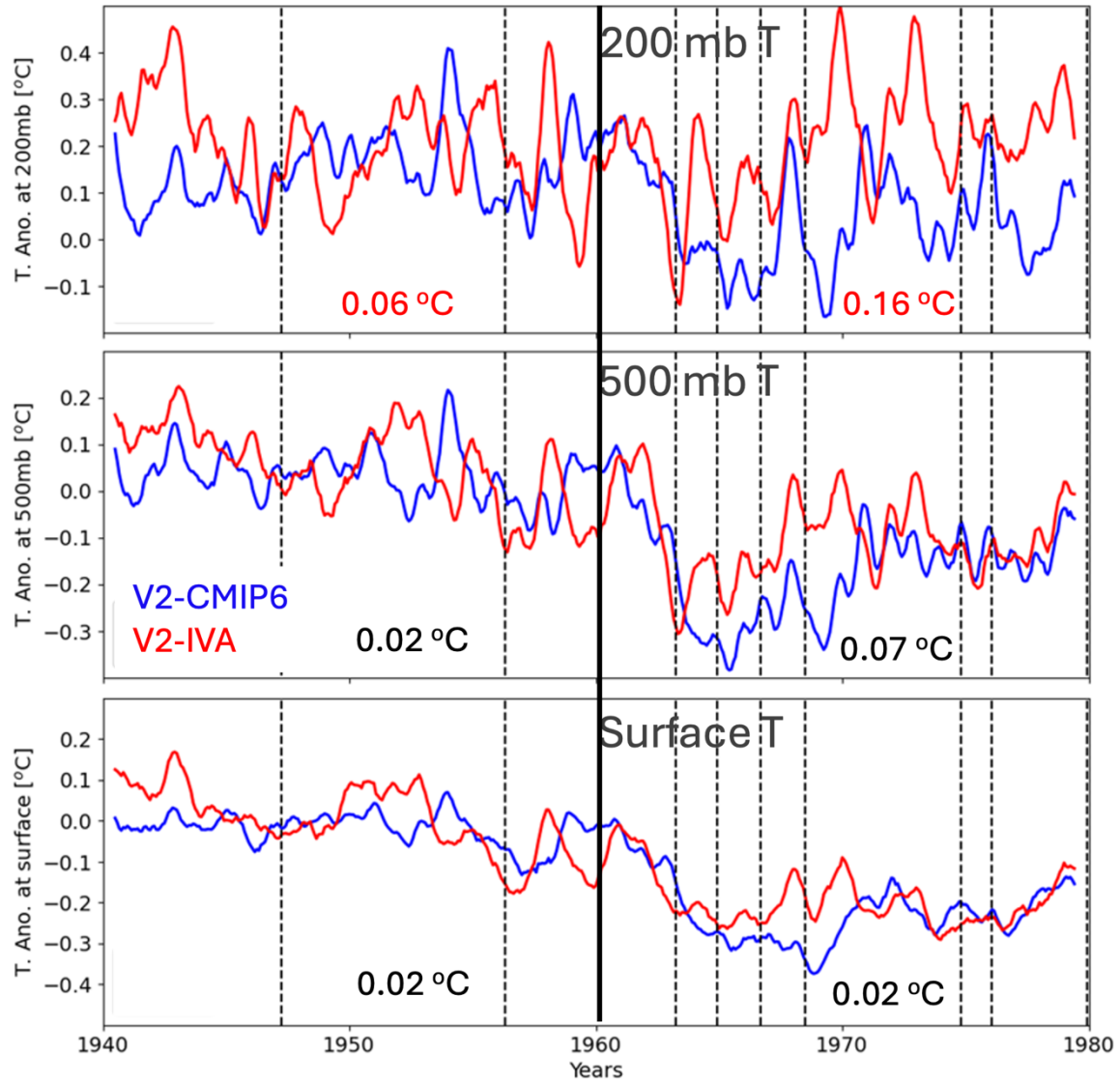
Figure 9. Time series of temperature anomaly at 200 hPa (*top*), 500 hPa (*middle*), and the surface (*bottom*). The dashed lines represent volcanic eruptions in volcanEESM (Table 2). The mean temperature differences during the 1940-1959 period between V2-IVA and V2-CMIP6 are shown in texts at the left side of all panels, while the differences during the 1960-1979 period are shown at the right side of all panels. The number of temperature difference in red color means it is significant with 95% confidence interval.
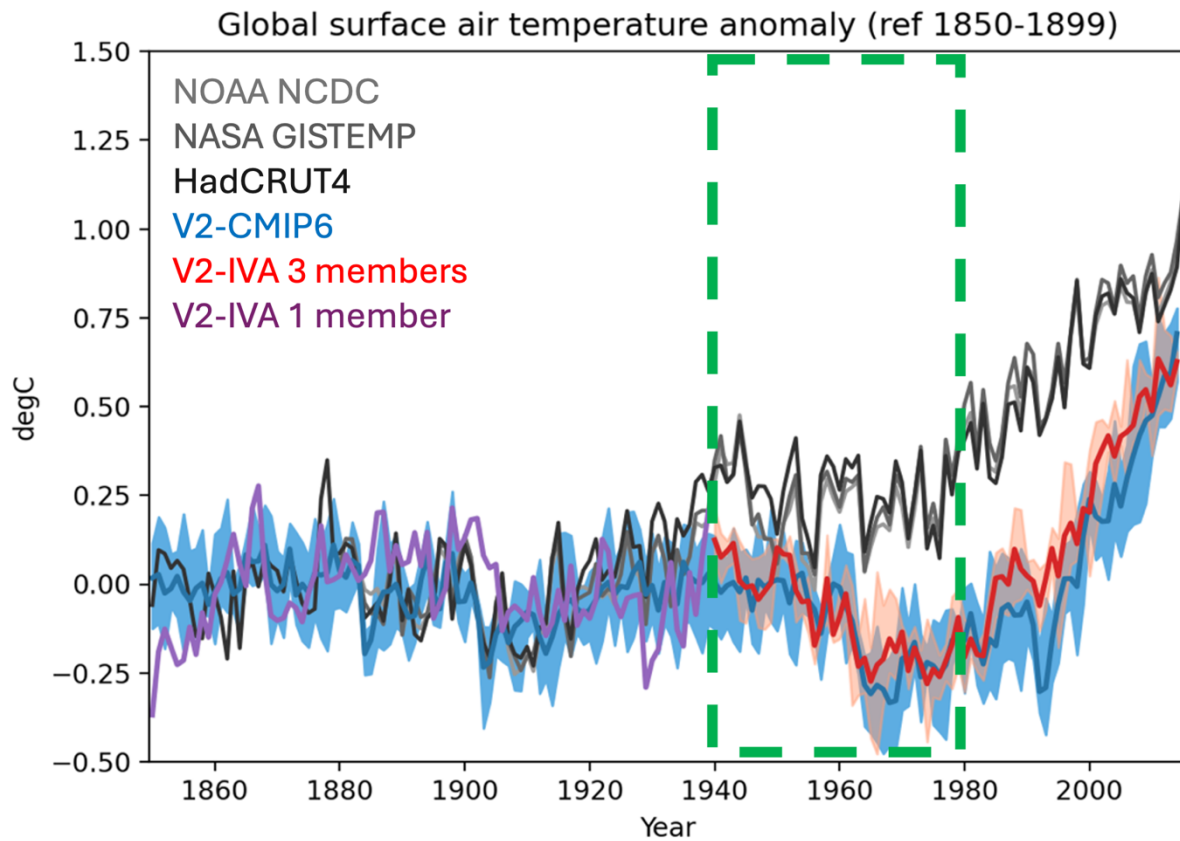
Figure 10. Temperature anomaly trends from 1850 to 2014. Black and gray lines represent observational data, blue line represents V2-CMIP6 ensemble mean, while red line represent V2-IVA ensemble mean during 1940-1980. The purple line represents the single member results of V2-IVA from 1850 to 1940.

653 **4   Conclusions and Discussion**

654   This study evaluates the impact of an improved volcanic sulfate aerosol representation in E3SM version 2 on mid-
655   20th-century climate simulations. By implementing an emission-based approach that accounts for both volcanic
656   sulfate aerosol-radiation interactions (VARIs) and volcanic sulfate aerosol-cloud interactions (VACIs), we aimed to
657   address the substantial surface temperature cold bias observed in E3SM historical simulations. The revised model
658   (V2-IVA) exhibits moderate improvements in surface temperature variability and a slightly warmer simulated
659   climate compared to the default CMIP6 volcanic forcing treatment (V2-CMIP6). The inclusion of additional
660   volcanic events, such as Hekla (1947) and Bezymianny (1956), enhances the representation of temperature
661   fluctuations, while the revised Mt. Agung eruption (1963) intensity and the more realistic treatment of VACIs
662   contribute to the slightly warmer climate simulated in V2-IVA. However, despite these improvements, the cold bias
663   in historical simulations remains largely uncorrected.

664   One key finding is that cloud forcing anomalies in V2-IVA are more consistent with expected aerosol-cloud
665   interaction processes. During the 1940–1959 period, when volcanic sulfate emissions (Av) were below the historical
666   average, cloud forcing anomalies were reduced relative to V2-CMIP6, leading to a warmer cloud cooling effect
667   (0.11 W/m^2). Conversely, during the 1960–1979 period, elevated volcanic sulfate emissions strengthened aerosol-
668   cloud interactions, resulting in a colder cooling effect (-0.07 W/m^2). This aligns with theoretical expectations based
669   on the aerosol increase ratio (R_v), as described in Equation 2. While these cloud forcing changes help explain some
670   differences in the temperature response, they are not sufficient to fully resolve the cold bias.

671   Several factors may explain why the temperature cold bias remains substantial. First, the overall aerosol cooling
672   effect in E3SM is approximately twice as strong as the CMIP6 multi-model mean (Golaz et al., 2022). This
673   discrepancy could be attributed to overestimation of aerosol burden. The E3SM development has incorporated the
674   interactive tropospheric chemistry to constrain sulfate aerosol production (Tang et al. in preparation) and enhanced
675   aerosol wet removal processes (Shan et al., 2021, 2024) for better scavenging. Additionally, while E3SMv2
676   implements the O3v2 model to better represent stratospheric ozone (Tang et al., 2021), its treatment of tropospheric
677   ozone lacks historical variability, potentially missing a warming contribution from tropospheric ozone changes
678   (Tang et al. in preparation). Another limitation is the use of the Liu and Penner (2005) scheme for homogeneous and
679   heterogeneous ice nucleation in cirrus clouds, which considers only sulfate aerosol particles in the Aitken mode,
680   potentially underestimates the impact on high clouds. Volcanic aerosols in the stratosphere rapidly grow from
681   Aitken to accumulation and even coarse mode when large eruptions occur, suggesting that ice nucleation from these
682   larger particles should be considered, as implemented in CESM2 (Visioni, 2017). Furthermore, one important
683   sources of background stratospheric sulfate, carbonyl sulfide (OCS), is not included in the current study. Missing
684   this source may lead to an underestimation of stratospheric sulfate aerosol levels, particularly during periods of low
685   volcanic activity, accounting for as much as one-third of the background sulfate burden in the stratosphere (Mills et
686   al., 2016). Addressing these limitations in future model versions could further improve the representation of aerosol-
687   climate interactions and help reduce the persistent temperature bias.

698   ***Code and data availability***
699   The dataset had been analyzed in this study are available at https://doi.org/10.5281/zenodo.11246313, E3SMv2
700   source code at https://doi.org/10.5281/zenodo.11403736 and E3SMv2 run script at
701   https://zenodo.org/records/11403988 The E3SM project, code, simulation configurations, model output and tools to

702 work with the output are described on the E3SM website (https://e3sm.org, last access: 20 May 2024). Instructions
703 on how to get started running E3SM and its components are available on the E3SM website
704 (https://e3sm.org/model/running-e3sm/e3sm-quick-start, last access: 20 May 2024).
705
706
707
708 *Competing interests*
709 At least one of the (co-)authors is a member of the editorial board of Geoscientific Model Development
710
711 *Author contribution*
712 All co-authors designed the experiments and Ziming Ke carried them out V2-IVA and V2-IVA-NPI experiments.
713 The V2-CMIP6 results had been provided by Jean-Christophe upon Golaz et al. (2022) study. Ziming Ke performed
714 the data analysis and all co-authors provided contributions. Ziming Ke prepared the manuscript with Xiaohong Liu
715 provided significant revisions. All co-authors contributed to final manuscript revisions.
716

717 *Acknowledgments*
718 This research was supported as part of the Energy Exascale Earth System Model (E3SM) project, funded by the US
719 Department of Energy (DOE), Office of Science, Office of Biological and Environmental Research (BER).
720 Lawrence Livermore National Laboratory (LLNL) is operated by Lawrence Livermore National Security, LLC, for
721 the US DOE, National Nuclear Security Administration under contract no. DEAC52-07NA27344. Support was
722 received from the LLNL LDRD project 22-ERD-008, "Multiscale Wildfire Simulation Framework and Remote
723 Sensing".
724
725
726 The Pacific Northwest National Laboratory (PNNL) is operated for DOE by Battelle Memorial Institute under
727 contract DE-AC05-76RLO1830.
728
729 We thank Paul J. Durack and Jiwoo Lee from LLNL for helping with manuscript discussion.
730
731 The data was produced using a high-performance computing cluster provided by the BER Earth System Modeling
732 program and operated by the Laboratory Computing Resource Center at Argonne National Laboratory.
733
734 The E3SM version 2.0 have been used in this study. The source code can be found at this link
735 (https://github.com/E3SM-Project/E3SM/releases/tag/v2.0.0. 29 Sep. 2021. Web.
736 doi:10.11578/E3SM/dc.20210927.1)
737

References

Arfeuille, F., Weisenstein, D., Mack, H., Rozanov, E., Peter, T., and Brönnimann, S.: Volcanic forcing for climate modeling: a new microphysics-based data set covering years 1600–present, Climate of the Past, 10, 359–375, https://doi.org/10.5194/cp-10-359-2014, 2014.

Bauer, S. E., Tsigaridis, K., Faluvegi, G., Kelley, M., Lo, K. K., Miller, R. L., Nazarenko, L., Schmidt, G. A., and Wu, J.: Historical (1850–2014) Aerosol Evolution and Role on Climate Forcing Using the GISS ModelE2.1 Contribution to CMIP6, Journal of Advances in Modeling Earth Systems, 12, e2019MS001978, https://doi.org/10.1029/2019MS001978, 2020.

Brown, H. Y., Wagman, B., Bull, D., Peterson, K., Hillman, B., Liu, X., Ke, Z., and Lin, L.: Validating a microphysical prognostic stratospheric aerosol implementation in E3SMv2 using observations after the Mount Pinatubo eruption, Geoscientific Model Development, 17, 5087–5121, https://doi.org/10.5194/gmd-17-5087-2024, 2024.

Chen, Y., Haywood, J., Wang, Y., Malavelle, F., Jordan, G., Peace, A., Partridge, D. G., Cho, N., Oreopoulos, L., Grosvenor, D., Field, P., Allan, R. P., and Lohmann, U.: Substantial cooling effect from aerosol-induced increase in tropical marine cloud cover, Nat. Geosci., 17, 404–410, https://doi.org/10.1038/s41561-024-01427-z, 2024.

Chim, M. M., Aubry, T. J., Abraham, N. L., Marshall, L., Mulcahy, J., Walton, J., and Schmidt, A.: Climate Projections Very Likely Underestimate Future Volcanic Forcing and Its Climatic Effects, Geophysical Research Letters, 50, e2023GL103743, https://doi.org/10.1029/2023GL103743, 2023.

Chylek, P., Folland, C., Klett, J. D., and Dubey, M. K.: CMIP5 Climate Models Overestimate Cooling by Volcanic Aerosols, Geophysical Research Letters, 47, e2020GL087047, https://doi.org/10.1029/2020GL087047, 2020.

Danabasoglu, G., Lamarque, J. -F., Bacmeister, J., Bailey, D. A., DuVivier, A. K., Edwards, J., Emmons, L. K., Fasullo, J., Garcia, R., Gettelman, A., Hannay, C., Holland, M. M., Large, W. G., Lauritzen, P. H., Lawrence, D. M., Lenaerts, J. T. M., Lindsay, K., Lipscomb, W. H., Mills, M. J., Neale, R., Oleson, K. W., Otto-Bliesner, B., Phillips, A. S., Sacks, W., Tilmes, S., Kampenhout, L., Vertenstein, M., Bertini, A., Dennis, J., Deser, C., Fischer, C., Fox-Kemper, B., Kay, J. E., Kinnison, D., Kushner, P. J., Larson, V. E., Long, M. C., Mickelson, S., Moore, J. K., Nienhouse, E., Polvani, L., Rasch, P. J., and Strand, W. G.: The Community Earth System Model Version 2 (CESM2), J. Adv. Model. Earth Syst., 12, https://doi.org/10.1029/2019MS001916, 2020.

Dhomse, S. S., Emmerson, K. M., Mann, G. W., Bellouin, N., Carslaw, K. S., Chipperfield, M. P., Hommel, R., Abraham, N. L., Telford, P., Braesicke, P., Dalvi, M., Johnson, C. E., O'Connor, F., Morgenstern, O., Pyle, J. A., Deshler, T., Zawodny, J. M., and Thomason, L. W.: Aerosol microphysics simulations of the Mt.~Pinatubo eruption with the UM-UKCA composition-climate model, Atmospheric Chemistry and Physics, 14, 11221–11246, https://doi.org/10.5194/acp-14-11221-2014, 2014.

Dhomse, S. S., Mann, G. W., Antuña Marrero, J. C., Shallcross, S. E., Chipperfield, M. P., Carslaw, K. S., Marshall, L., Abraham, N. L., and Johnson, C. E.: Evaluating the simulated radiative forcings, aerosol properties, and stratospheric warmings from the 1963 Mt Agung, 1982 El Chichón, and 1991 Mt Pinatubo volcanic aerosol clouds, Atmospheric Chemistry and Physics, 20, 13627–13654, https://doi.org/10.5194/acp-20-13627-2020, 2020.

Eyring, V., Bony, S., Meehl, G. A., Senior, C. A., Stevens, B., Stouffer, R. J., and Taylor, K. E.: Overview of the Coupled Model Intercomparison Project Phase 6 (CMIP6) experimental design and organization, Geosci. Model Dev., 9, 1937–1958, https://doi.org/10.5194/gmd-9-1937-2016, 2016.

Flynn, C. M. and Mauritsen, T.: On the climate sensitivity and historical warming evolution in recent coupled model ensembles, Atmospheric Chemistry and Physics, 20, 7829–7842, https://doi.org/10.5194/acp-20-7829-2020, 2020.

Golaz, J., Van Roekel, L. P., Zheng, X., Roberts, A. F., Wolfe, J. D., Lin, W., Bradley, A. M., Tang, Q., Maltrud, M. E., Forsyth, R. M., Zhang, C., Zhou, T., Zhang, K., Zender, C. S., Wu, M., Wang, H., Turner, A. K., Singh, B., Richter, J. H., Qin, Y., Petersen, M. R., Mametjanov, A., Ma, P., Larson, V. E., Krishna, J., Keen, N. D., Jeffery, N., Hunke, E. C., Hannah, W. M., Guba, O., Griffin, B. M., Feng, Y., Engwirda, D., Di Vittorio, A. V., Dang, C., Conlon, L. M., Chen, C., Brunke, M. A., Bisht, G., Benedict, J. J., Asay-Davis, X. S., Zhang, Y., Zhang, M., Zeng, X., Xie, S., Wolfram, P. J., Vo, T., Veneziani, M., Tesfa, T. K., Sreepathi, S., Salinger, A. G., Reeves Eyre, J. E. J., Prather, M. J., Mahajan, S., Li, Q., Jones, P. W., Jacob, R. L., Huebler, G. W., Huang, X., Hillman, B. R., Harrop, B. E., Foucar, J. G., Fang, Y., Comeau, D. S., Caldwell, P. M., Bartoletti, T., Balaguru, K., Taylor, M. A., McCoy, R. B., Leung, L. R., and Bader, D. C.: The DOE E3SM Model Version 2: Overview of the Physical Model and Initial Model Evaluation, J Adv Model Earth Syst, 14, https://doi.org/10.1029/2022MS003156, 2022.

Guo, H., Golaz, J.-C., Donner, L. J., Wyman, B., Zhao, M., and Ginoux, P.: CLUBB as a unified cloud parameterization: Opportunities and challenges, Geophysical Research Letters, 42, 4540–4547, https://doi.org/10.1002/2015GL063672, 2015.

Hegerl, G. C., Crowley, T. J., Baum, S. K., Kim, K.-Y., and Hyde, W. T.: Detection of volcanic, solar and greenhouse gas signals in paleo-reconstructions of Northern Hemispheric temperature, Geophysical Research Letters, 30, https://doi.org/10.1029/2002GL016635, 2003.

Holtslag, A. a. M. and Boville, B. A.: Local Versus Nonlocal Boundary-Layer Diffusion in a Global Climate Model, Journal of Climate, 6, 1825–1842, https://doi.org/10.1175/1520-0442(1993)006<1825:LVNBLD>2.0.CO;2, 1993.

Liu, X. and Penner, J. E.: Ice nucleation parameterization for global models, metz, 14, 499–514, https://doi.org/10.1127/0941-2948/2005/0059, 2005.

Liu, X., Easter, R. C., Ghan, S. J., Zaveri, R., Rasch, P., Shi, X., Lamarque, J.-F., Gettelman, A., Morrison, H., Vitt, F., Conley, A., Park, S., Neale, R., Hannay, C., Ekman, A. M. L., Hess, P., Mahowald, N., Collins, W., Iacono, M. J., Bretherton, C. S., Flanner, M. G., and Mitchell, D.: Toward a minimal representation of aerosols in climate models: description and evaluation in the

Community Atmosphere Model CAM5, Geosci. Model Dev., 5, 709–739,
https://doi.org/10.5194/gmd-5-709-2012, 2012.

Malavelle, F. F., Haywood, J. M., Jones, A., Gettelman, A., Clarisse, L., Bauduin, S., Allan, R.
P., Karset, I. H. H., Kristjánsson, J. E., Oreopoulos, L., Cho, N., Lee, D., Bellouin, N., Boucher,
O., Grosvenor, D. P., Carslaw, K. S., Dhomse, S., Mann, G. W., Schmidt, A., Coe, H., Hartley,
M. E., Dalvi, M., Hill, A. A., Johnson, B. T., Johnson, C. E., Knight, J. R., O'Connor, F. M.,
Partridge, D. G., Stier, P., Myhre, G., Platnick, S., Stephens, G. L., Takahashi, H., and
Thordarson, T.: Strong constraints on aerosol–cloud interactions from volcanic eruptions,
Nature, 546, 485–491, https://doi.org/10.1038/nature22974, 2017.

Mills, M. J., Schmidt, A., Easter, R., Solomon, S., Kinnison, D. E., Ghan, S. J., Neely, R. R.,
Marsh, D. R., Conley, A., Bardeen, C. G., and Gettelman, A.: Global volcanic aerosol properties
derived from emissions, 1990-2014, using CESM1(WACCM): VOLCANIC AEROSOLS
DERIVED FROM EMISSIONS, J. Geophys. Res. Atmos., 121, 2332–2348,
https://doi.org/10.1002/2015JD024290, 2016.

Mills, M. J., Richter, J. H., Tilmes, S., Kravitz, B., MacMartin, D. G., Glanville, A. A., Tribbia,
J. J., Lamarque, J.-F., Vitt, F., Schmidt, A., Gettelman, A., Hannay, C., Bacmeister, J. T., and
Kinnison, D. E.: Radiative and Chemical Response to Interactive Stratospheric Sulfate Aerosols
in Fully Coupled CESM1(WACCM), Journal of Geophysical Research: Atmospheres, 122,
13,061-13,078, https://doi.org/10.1002/2017JD027006, 2017.

Morrison, H. and Gettelman, A.: A New Two-Moment Bulk Stratiform Cloud Microphysics
Scheme in the Community Atmosphere Model, Version 3 (CAM3). Part I: Description and
Numerical Tests, Journal of Climate, 21, 3642–3659, https://doi.org/10.1175/2008JCLI2105.1,
2008.

Neely, R. R. and Schmidt, A.: VolcanEESM: Global volcanic sulphur dioxide (SO2) emissions
database from 1850 to present - Version 1.0, 2016.

Niemeier, U., Timmreck, C., and Krüger, K.: Revisiting the Agung 1963 volcanic forcing –
impact of one or two eruptions, Atmospheric Chemistry and Physics, 19, 10379–10390,
https://doi.org/10.5194/acp-19-10379-2019, 2019.

Raible, C. C., Brönnimann, S., Auchmann, R., Brohan, P., Frölicher, T. L., Graf, H.-F., Jones, P.,
Luterbacher, J., Muthers, S., Neukom, R., Robock, A., Self, S., Sudrajat, A., Timmreck, C., and
Wegmann, M.: Tambora 1815 as a test case for high impact volcanic eruptions: Earth system
effects, WIREs Climate Change, 7, 569–589, https://doi.org/10.1002/wcc.407, 2016.

Ramachandran, S., Ramaswamy, V., Stenchikov, G. L., and Robock, A.: Radiative impact of the
Mount Pinatubo volcanic eruption: Lower stratospheric response, Journal of Geophysical
Research: Atmospheres, 105, 24409–24429, https://doi.org/10.1029/2000JD900355, 2000.

Rieger, L. A., Cole, J. N. S., Fyfe, J. C., Po-Chedley, S., Cameron-Smith, P. J., Durack, P. J.,
Gillett, N. P., and Tang, Q.: Quantifying CanESM5 and EAMv1 sensitivities to Mt. Pinatubo
volcanic forcing for the CMIP6 historical experiment, Geosci. Model Dev., 13, 4831–4843,
https://doi.org/10.5194/gmd-13-4831-2020, 2020.

855   Schmidt, A., Carslaw, K. S., Mann, G. W., Rap, A., Pringle, K. J., Spracklen, D. V., Wilson, M.,
856   and Forster, P. M.: Importance of tropospheric volcanic aerosol for indirect radiative forcing of
857   climate, Atmospheric Chemistry and Physics, 12, 7321–7339, https://doi.org/10.5194/acp-12-
858   7321-2012, 2012.

859   Schmidt, A., Mills, M. J., Ghan, S., Gregory, J. M., Allan, R. P., Andrews, T., Bardeen, C. G.,
860   Conley, A., Forster, P. M., Gettelman, A., Portmann, R. W., Solomon, S., and Toon, O. B.:
861   Volcanic Radiative Forcing From 1979 to 2015, Journal of Geophysical Research: Atmospheres,
862   123, 12491–12508, https://doi.org/10.1029/2018JD028776, 2018.

863   Shan, Y., Liu, X., Lin, L., Ke, Z., and Lu, Z.: An improved representation of aerosol wet removal
864   by deep convection and impacts on simulated aerosol vertical profiles, Journal of Geophysical
865   Research: Atmospheres, 126, e2020JD034173, 2021.

866   Shan, Y., Fan, J., Zhang, K., Shpund, J., Terai, C., Zhang, G. J., Song, X., Chen, C.-C.-J., Lin,
867   W., Liu, X., Shrivastava, M., Wang, H., and Xie, S.: Improving Aerosol Radiative Forcing and
868   Climate in E3SM: Impacts of New Cloud Microphysics and Improved Wet Removal Treatments,
869   Journal of Advances in Modeling Earth Systems, 16, e2023MS004059,
870   https://doi.org/10.1029/2023MS004059, 2024.

871   Smith, K. L., Neely, R. R., Marsh, D. R., and Polvani, L. M.: The Specified Chemistry Whole
872   Atmosphere Community Climate Model (SC-WACCM), J. Adv. Model. Earth Syst., 6, 883–901,
873   https://doi.org/10.1002/2014MS000346, 2014.

874   Thomason, L. W., Ernest, N., Millán, L., Rieger, L., Bourassa, A., Vernier, J.-P., Manney, G.,
875   Luo, B., Arfeuille, F., and Peter, T.: A global space-based stratospheric aerosol climatology:
876   1979–2016, Earth System Science Data, 10, 469–492, https://doi.org/10.5194/essd-10-469-2018,
877   2018.

878   Timmreck, C., Graf, H.-F., Lorenz, S. J., Niemeier, U., Zanchettin, D., Matei, D., Jungclaus, J.
879   H., and Crowley, T. J.: Aerosol size confines climate response to volcanic super-eruptions,
880   Geophysical Research Letters, 37, https://doi.org/10.1029/2010GL045464, 2010.

881   Vignesh, P. P., Jiang, J. H., Kishore, P., Su, H., Smay, T., Brighton, N., and Velicogna, I.:
882   Assessment of CMIP6 Cloud Fraction and Comparison with Satellite Observations, Earth and
883   Space Science, 7, e2019EA000975, https://doi.org/10.1029/2019EA000975, 2020.

884   Visioni, D., Pitari, G., Aquila, V., Tilmes, S., Cionni, I., Di Genova, G., and Mancini, E.: Sulfate
885   geoengineering impact on methane transport and lifetime: results from the Geoengineering
886   Model Intercomparison Project (GeoMIP), Atmos. Chem. Phys., 17, 11209–11226,
887   https://doi.org/10.5194/acp-17-11209-2017, 2017.

888   Wang, H., Wu, M., Liu, X., Yang, K., Shi, Y., Darmenov, A., Yu, H., Wang, Z., Luo, T., and
889   Feng, Y.: Evaluation of dust emission and transport simulated by global climate models with
890   satellite observations from CALIOP, MODIS, and MISR, in: AGU Fall Meeting Abstracts,
891   A31R-2752, 2019.

892 Wang, Y., Liu, X., Hoose, C., and Wang, B.: Different contact angle distributions for
893 heterogeneous ice nucleation in the Community Atmospheric Model version 5, Atmos. Chem.
894 Phys., 14, 10411–10430, https://doi.org/10.5194/acp-14-10411-2014, 2014.

895 Wang, Y.-C., Xie, S., Tang, S., and Lin, W.: Evaluation of an Improved Convective Triggering
896 Function: Observational Evidence and SCM Tests, Journal of Geophysical Research:
897 Atmospheres, 125, e2019JD031651, https://doi.org/10.1029/2019JD031651, 2020.

898 Zanchettin, D., Khodri, M., Timmreck, C., Toohey, M., Schmidt, A., Gerber, E. P., Hegerl, G.,
899 Robock, A., Pausata, F. S. R., Ball, W. T., Bauer, S. E., Bekki, S., Dhomse, S. S., LeGrande, A.
900 N., Mann, G. W., Marshall, L., Mills, M., Marchand, M., Niemeier, U., Poulain, V., Rozanov, E.,
901 Rubino, A., Stenke, A., Tsigaridis, K., and Tummon, F.: The Model Intercomparison Project on
902 the climatic response toVolcanic forcing (VolMIP): experimental design and forcing input data
903 for CMIP6, Geosci. Model Dev., 9, 2701–2719, https://doi.org/10.5194/gmd-9-2701-2016, 2016.

904 Zhang, G. J. and McFarlane, N. A.: Sensitivity of climate simulations to the parameterization of
905 cumulus convection in the Canadian climate centre general circulation model, Atmosphere-
906 Ocean, 33, 407–446, https://doi.org/10.1080/07055900.1995.9649539, 1995.

907 Zhang, J., Furtado, K., Turnock, S. T., Mulcahy, J. P., Wilcox, L. J., Booth, B. B., Sexton, D.,
908 Wu, T., Zhang, F., and Liu, Q.: The role of anthropogenic aerosols in the anomalous cooling
909 from 1960 to 1990 in the CMIP6 Earth system models, Atmospheric Chemistry and Physics, 21,
910 18609–18627, https://doi.org/10.5194/acp-21-18609-2021, 2021.

911 Zhang, K., Zhang, W., Wan, H., Rasch, P. J., Ghan, S. J., Easter, R. C., Shi, X., Wang, Y.,
912 Wang, H., Ma, P.-L., Zhang, S., Sun, J., Burrows, S. M., Shrivastava, M., Singh, B., Qian, Y.,
913 Liu, X., Golaz, J.-C., Tang, Q., Zheng, X., Xie, S., Lin, W., Feng, Y., Wang, M., Yoon, J.-H.,
914 and Leung, L. R.: Effective radiative forcing of anthropogenic aerosols in E3SM version 1:
915 historical changes, causality, decomposition, and parameterization sensitivities, Atmospheric
916 Chemistry and Physics, 22, 9129–9160, https://doi.org/10.5194/acp-22-9129-2022, 2022.

917